PHYSICAL REVIEW B **92**, 024104 (2015)

Charge localization in the Verwey structure of magnetite

Mark S. Senn,[1] Jon P. Wright,[2] James Cumby,[3] and J. Paul Attfield[3,*]
[1]*Inorganic Chemistry Laboratory, University of Oxford, South Parks Road, Oxford, OX1 3QR, United Kingdom*
[2]*European Synchrotron Radiation Facility, 6 rue Jules Horowitz, Grenoble Cedex 9, 38000 France*
[3]*Centre for Science at Extreme Conditions and School of Chemistry, University of Edinburgh, West Mains Road, Edinburgh, EH9 3JZ, United Kingdom*

(Received 9 April 2015; published 7 July 2015)

The thermal evolution of electronic order in the complex Verwey ground state of magnetite (Fe_3O_4) has been determined through 22 high-accuracy synchrotron x-ray structure refinements using three 10–40 μm grains of stoichiometric magnetite. A robust fitting function is introduced to extract values of order parameterlike quantities at zero temperature and at the upper limit of the Verwey phase $T_u = 123.4$ K. The low-temperature structural distortion is found to be almost frozen below the Verwey transition but small changes in lattice and local mode amplitudes and Fe-Fe distances reveal an increase in electron localization on cooling. These distortions confirm that electron localization within trimerons is the driving force behind the Verwey transition. Electron localization is also revealed by anomalous decreases in the largest principal thermal displacement factors of Fe cations as electron-phonon decoupling occurs on cooling.

DOI: 10.1103/PhysRevB.92.024104 PACS number(s): 64.60.Ej, 75.25.Dk, 64.70.K−, 61.66.−f

I. INTRODUCTION

The physical properties of magnetite (Fe_3O_4) as a magnetic oxide with large room-temperature magnetization and spin-polarized conductivity are of continuing interest. At ambient temperatures magnetite has the cubic AB_2O_4 spinel structure (space group $Fd\bar{3}m$) with inverse formal charge distribution $Fe^{3+}(Fe^{2.5+})_2O_4$. However, a more complex superstructure is adopted below the Verwey transition at $T_V \approx 125$ K and the electronic ground state has been investigated for over 75 years since Verwey proposed that this is driven by charge ordering of Fe^{2+} and Fe^{3+} ions over the octahedral B-type sites in the spinel lattice [1–3]. This order was not verified during the early decades of study due to the complexity of the low-temperature superstructure, which has monoclinic Cc space group symmetry, and to microtwinning of Cc domains. More recent structure refinements [4–7] and Fe K-edge resonant x-ray studies [8–12] provided evidence for charge order in some cases but these used approximate structural models in which the supercell symmetry or displacement amplitudes were simplified.

An unconstrained experimental refinement of all 168 atomic coordinates in the full Cc supercell of magnetite was recently achieved through use of microcrystal x-ray diffraction [13]. Small ($<100\,\mu$m) magnetite grains were used so that few domain orientations are formed in the low-temperature phase, and the diffraction data sets were analyzed using software for twinned crystals. The published structure was obtained from a 40 μm grain at 90 K containing only two domain orientations, in an 89:11 ratio. Fe^{2+}/Fe^{3+} charge ordering and orbital ordering of degenerate $t_{2g}^4 e_g^2$ Fe^{2+} states were evidenced from analysis of the observed Fe-O distances, confirming that Verwey's charge ordering hypothesis [1] is correct to a useful first approximation. However, additional structural distortions in which B-site Fe-Fe distances within linear Fe-Fe-Fe units are anomalously shortened showed that electrons are not fully localized as Fe^{2+} states, but are instead spread over the three sites resulting in highly structured three-site polarons known as trimerons. These are an example of orbital molecules, weakly bonded clusters of orbitally ordered cations [14]. The real-space density distribution of the localized electrons, calculated from the experimental coordinates by the DFT + U method, supports the trimeron description [15]. The complex ordering pattern of the trimerons gives rise to multiple superimposed atomic displacements so that the overall structural distortion has significant contributions from many of the 168 frozen phonon modes, in particular with Δ_5, X_1, X_4, and W_1 symmetries [16]. The deduced charge, orbital, and trimeron orders are shown in Fig. 1

The trimeron model for the ground state of magnetite has been used to account for the ferroelectric properties as large atomic displacements of some Fe^{3+} ions due to cooperative trimeron order result in a large predicted ferroelectric polarization [13]. A characteristic 300 fs timescale for the destruction of trimerons has been reported to be the first step to metallization of the Verwey state under intense laser irradiation [17]. The complexity of the low-temperature electronic order in magnetite raises the question of whether some changes may occur between zero temperature and the Verwey transition through electron-phonon coupling. NMR has shown some temperature dependence of the Fe-site resonances within the Verwey phase [18]. In order to discover any changes in the complex Verwey structure with temperature, we report here a detailed x-ray study of the Cc superstructure of magnetite between 20 K and the Verwey transition.

II. EXPERIMENTAL

The powder and microcrystals of magnetite were taken from the same high-quality sample used in previous studies [5,6,8,13]. To extract accurate values of the lattice parameters for the Verwey phase, high-resolution powder x-ray diffraction data were collected on beam line ID31 at the ESRF. Diffraction patterns were collected between 5 and 124 K in

---

[*] Corresponding author: j.p.attfield@ed.ac.uk

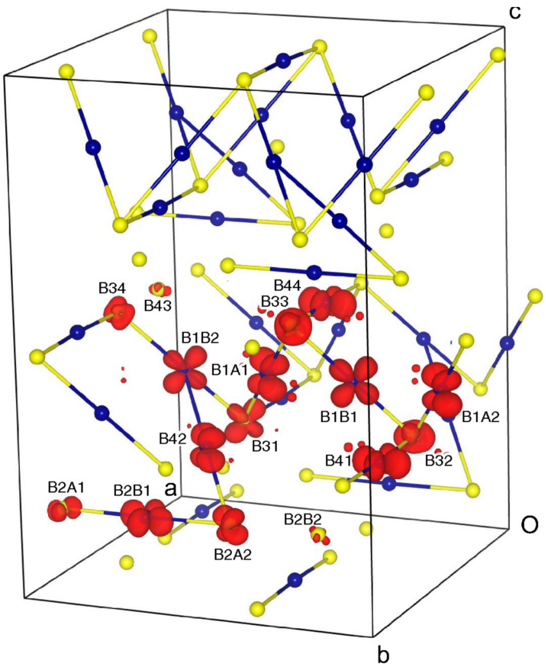

FIG. 1. (Color online) The low-temperature Cc unit cell of magnetite with B site Fe^{2+}/Fe^{3+}-like states drawn as blue/yellow spheres, and trimeron connections between B sites shown. Each of the 16 unique B sites is labeled once with minority spin density calculated in Ref. [15] shown.

the angular range $2\theta = 4.5^\circ$–26.0° and were analyzed using the GSAS program with EXPGUI interface [19,20]. The wavelength of 0.3997592(11) Å was calibrated using NIST 640c silicon standard.

Microcrystal diffraction data were collected on instrument ID11 at ESRF. The experimental procedure was the same as used in Refs. [13,17]. Microcrystals with radii in the range 10–40 μm were initially screened for diffraction quality at room temperature, and four were selected for low-temperature study. Measurements were performed on warming from a base temperature of 20 K using a helium cryostream cooler, or from 80 K with a nitrogen cryostream. A thermocouple was used to measure the nitrogen stream temperatures, and the phase transition in $TbAsO_4$ was used previously to confirm the temperature calibration of the helium cooler. Thirty-one full data sets consisting of ~90 000 symmetry unique reflections out to a resolution of 0.30 Å were collected from the four microcrystals in the temperature range 20–126 K. Data reduction was performed using SMART/SAINT software, empirical absorption correction applied in SADABS and incidence angle corrections were performed [21].

Structure refinements were performed in SHELXL [22] taking our previously published model as the initial starting coordinates [13], and using sequentially converged coordinates as the initial input for subsequent refinements. All atomic coordinates were refined freely in space group Cc. Refinements were performed with anisotropic thermal parameters for Fe sites and isotropic parameters for O atoms. The total number of refined parameters including $a/{-a}$ and a/b type twin domain fractions was 349.

The 31 structure refinements had R_1 residual values ranging from 2.72 to 5.16%. We selected an R_1 threshold of 4.0% to exclude the less accurate models, which left 22 refinements from three different crystals (Crystals 8, 11, and 17) spanning the temperature range 20–124 K. Crystals 8 and 11 had significant fractions of four monoclinic domains due to $a/{-a}/b/{-b}$ twinning, whereas Crystal 17 had predominantly just the two $a/{-a}$ domains. Across all 22 models, only one thermal parameter refined to be nonpositive definite indicating the quality and stability of our refinements. Refinements near 90 K are in excellent agreement with our previously published model. Lattice parameters for the 22 models were taken from the powder diffraction results, using linear interpolation where powder data were not collected at matching temperatures. Distortion mode amplitudes, bond distances, and principal mean-square atomic displacements were calculated from the converged atomic coordinates and thermal displacement parameters, and their evolution with temperature is discussed below. Estimated standard deviations in mode amplitudes and bond distances are $<2 \times 10^{-3}$ Å. Cif files from the SHELXL refinements are available as Supplemental Material [23].

III. RESULTS AND DISCUSSION

A. Order parameter variations

The Verwey transition leads to a first-order structural change from the high-temperature cubic spinel-type form of magnetite (space group $Fd\bar{3}m$) to the low-temperature phase, which has a $\sqrt{2} \times \sqrt{2} \times 2$ superstructure with monoclinic Cc symmetry. To analyze thermal variations in structural quantities we start from the simplest Landau theory description of a first-order phase transition at temperature T_c. This uses an expansion of the Gibbs free-energy difference between high- and low-temperature phases G, assumed to be symmetric under inversion of the order parameter X, up to sixth order [24];

$$G = (1/2)A(T - T_c)X^2 + (1/4)BX^4 + (1/6)CX^6. \quad (1)$$

For coefficients $A > 0$, $B < 0$, and $C > 0$ a first-order transition is predicted with nonzero X in the temperature range $0 < T < T_u$, where the upper temperature limit for the low-temperature phase is $T_u = T_c + (B^2/4AC)$, and the high- and low-temperature phases coexist at $T_c < T < T_u$. For small values of the reduced temperature $t_u = (T_u - T)/T_u$, the order parameter varies as;

$$X = X_u + (X_0 – X_u){t_u}^{1/2}, \quad (2)$$

where $X_u = \sqrt{-B/2C}$ and $X_0 = \sqrt{(-B/2C)}[1–\sqrt{(ACT_u)}]$ are, respectively, values of X at T_u and at $T = 0$.

Critical equations such as (2) describe order parameter variations close to the transition accurately, but overestimate X_0 when extrapolated to low temperatures [25]. For practical data-fitting purposes it is useful to find a function that fits X over the entire $0 < T < T_u$ temperature range while still approximating to a critical law close to the transition. We have found that the empirical function;

$$X = X_u + (X_0 – X_u)\tanh\left(W_X t_u^{\beta}\right)/\tanh(W_X) \quad (3)$$

assuming exponent $\beta = 1/2$, gives a good fit to thermal variations of order parameterlike structural quantities (varying as

X or $X+$ constant); lattice parameters, interatomic distances, distortion mode amplitudes, root mean square displacements, as shown in the following sections of this paper. This function with $\beta = 1/2$ approximates to Eq. (2) at small t_u, and provides a useful empirical correction for the contribution of higher-order terms to the excess free energy in Eq. (1) at large t_u through the additional fitting parameter W_X. Function (3) was found to be mathematically robust and to give a good description of parameter variations from low temperatures (4–20 K) up to $T_u = 123.4$ K. W_X typically converged to values between 1.5 and 4 and a fixed value of $W_X = 2$ was used in some fits to noisy data variations. However, the value of the exponent β could not be determined independently in these fits and $\beta = 1/2$ is assumed throughout.

Two limiting behaviors for first-order transitions can be identified using the magnitudes of the fitted parameters X_0 and X_u. Quasicontinuous transitions have $|X_0–X_u| \gg |X_u|$, and become continuous when $X_u = 0$, whereas frozen transitions have $|X_0–X_u| \ll |X_u|$ with very little thermal change in the order parameter below T_u so that $X_0 \approx X_u$. For fits to many X variables such as the 168 mode amplitudes in the low-temperature magnetite structure, the plot of X_u against X_0 is useful to distinguish frozen behavior ($X_u/X_0 \approx 1$) from quasicontinuous ($X_u/X_0 \approx 0$). Magnetite is close to the frozen limit as illustrated by plots in the following sections.

B. Lattice parameters

Clear peak splittings are observed at the Verwey transition in the powder x-ray diffraction patterns of magnetite, as shown in Fig. 2(a). Although the transition is sharp, residual weak intensity at cubic peak positions was observed down to ~80 K. This probably results from suppression of the Verwey transition in some crystallites due to strains from the surrounding transformed regions. The reduction in the lattice parameter of this residual stressed cubic component on cooling (Fig. 3) shows that it is probably not an effect of the beam heating effect due to the high x-ray flux, which would be an alternative explanation for observation of the high-temperature phase. Two phase fits were used to extract monoclinic and cubic phase fractions from the powder patterns. By drawing a line through the steepest descent of the monoclinic phase fraction, see Fig. 2(b), the structural transition width is estimated to be 2.0 K with lower and upper limits of T_c ($=T_V$) = 121.4 K and $T_u = 123.4$ K. These are in keeping with previous reports of $T_V = 120–125$ K in stoichiometric magnetite [26].

Temperature variations of the lattice parameters are shown in Fig. 3. Equation (3) gives good fits to all the monoclinic lattice parameters and the fitting values are shown in Table I. Cell lengths, volume, and cos β are used here for convenience, but Eq. (3) can also be used to fit lattice strains as used elsewhere for the low-temperature cell [27]. The X_0 values give the best experimental estimates of the $T = 0$ ground-state lattice parameters of magnetite reported to date. W_X values are consistent with the representation properties of the axes under monoclinic symmetry, as $W_a \approx W_c$ while W_b has a different value. Also $W_b \approx W_v$, where $v = (\text{Volume}/4)^{1/3}$ is the pseudocubic cell parameter of the monoclinic phase, showing that volume variation follows the unique b axis, despite the similar magnitudes of ($X_0–X_u$) differences for the three normalized cell lengths. These observations demonstrate that the W parameters have some physical significance despite parametrizing an empirical correction to describe behavior at large t_u.

TABLE I. Parameters from fits of Eq. (3) to the lattice parameters in Fig. 3 with fitting errors in parentheses.

X	X_0	X_c	W_X
$a/\sqrt{2}$ (Å)	8.40767(5)	8.40501(7)	2.09(9)
$b/\sqrt{2}$ (Å)	8.37759(5)	8.38188(7)	1.40(5)
$c/2$ (Å)	8.38825(5)	8.39150(7)	1.99(7)
cos β	−0.004076(4)	−0.003928(8)	3.256(1)
$(\text{Volume}/4)^{1/3}$ Å	8.39113(4)	8.39277(4)	1.410(2)

The cell volume of magnetite shows very little thermal expansion below T_V compared to that at higher temperatures [28], so critical variations are assumed to outweigh thermal effects on length order parameters throughout this paper.

C. Atomic parameters and lattice modes

Amplitudes q of the 168 coherent displacement modes in the low-temperature Cc structure of magnetite, relative to the high-temperature $Fd\bar{3}m$ spinel arrangement, were calculated from the refined coordinates as in our previous studies [29]. The modes fall into four symmetry

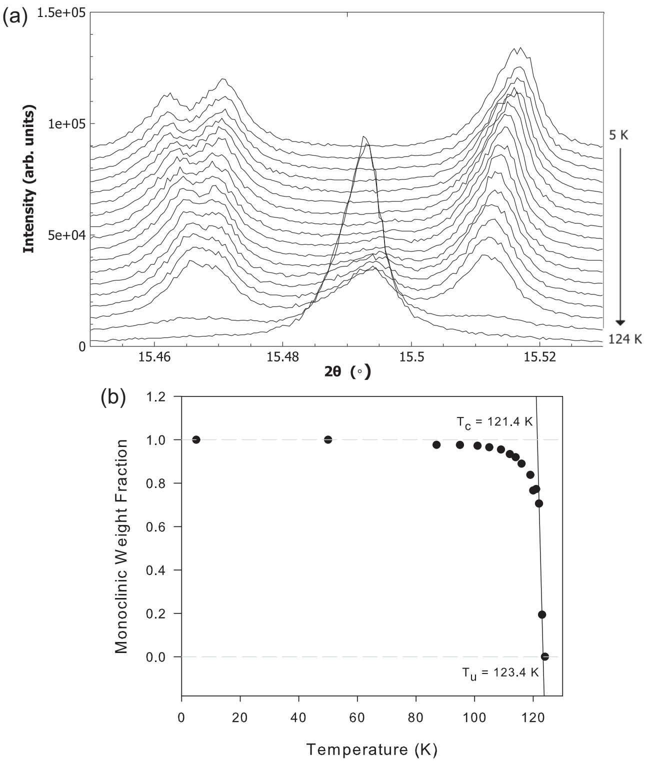

FIG. 2. (a) Variable temperature powder x-ray diffraction patterns for magnetite showing the cubic (440) peak at $2\theta = 15.49^\circ$ and split components from the low temperature monoclinic phase. (b) Temperature evolution of the monoclinic phase fraction.

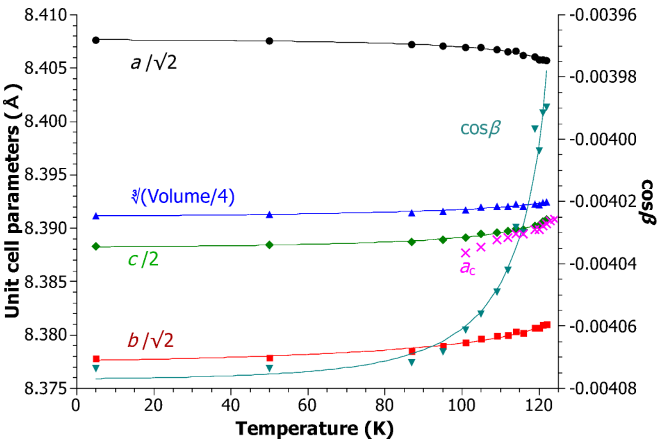

FIG. 3. (Color online) Thermal variation of the lattice parameters of magnetite showing fits of Eq. (3) to the monoclinic phase values.

classes; Γ, Δ, X, and W. Temperature variation of the mode amplitudes was fitted using Eq. (3) and some representative plots are shown in Fig. 4(a). The plot of $T = T_u$ values q_u against $T = 0$ values q_0 for the 168 modes in Fig. 4(b) shows that all four classes exhibit near frozen behavior with $q_u/q_0 \approx 0.9$. There is no significant difference in q_u/q_0 behavior between the different symmetry classes, or between small and large amplitude modes. However, the deviations of some modes from the average trend reflect the small structural changes due to electronic relaxation of the structure below T_V, as discussed in the next section.

Vibrational motion of Fe atoms in the *Cc* magnetite structure refinements were described by anisotropic U_{ij} thermal displacement parameters, from which the three root mean squared displacements (RMSDs) in the directions of the principal axes of the thermal displacement ellipsoid were obtained. For the *B* cation Fe sites, one RMSD was found to be significantly greater than the other two at high temperatures near T_u, but this value decreases on cooling so that the three RMSDs are near equal at $T = 0$. Mean-squared displacements $\langle U^2\rangle$ near a phase transition are determined by renormalized static phonon frequencies and a $\langle U^2\rangle \sim t^{2\beta}$ variation is expected just below the transition [30]. Hence RMSD $(=\sqrt{\langle U^2\rangle})$ is expected to vary with $t_u^{1/2}$ in the critical region for magnetite assuming exponent $\beta = 1/2$, so Eq. (3) provides an appropriate description although RMSDs are not formally order parameters. Thermal variation of RMSDs was found to be described well by Eq. (3) as shown in Fig. 5(a), and values at T_u are plotted against $T = 0$ values for the largest RMSD of each *B* site atom in Fig. 5(b).

The anomalous increase in the largest *B*-site RMSDs as *T* approaches T_u shown in Fig. 5 demonstrates that coupling of the minority spin *B*-site electrons to the lattice results in activation of phonon modes, or in additional disordered static displacements, as the transition is approached. Figure 5(b) shows that the RMSDs at $T = T_u$ exceed the $T = 0$ values of ∼0.05 Å from zero-point thermal motion by up to 0.03 Å. This corresponds to the excitation of additional dynamic or disordered static RMS displacements of up to ∼0.06 Å per *B* cation, which is comparable to half the magnitude of changes in *B*-*B* distances associated with trimeron formation, as discussed in Sec. III E.

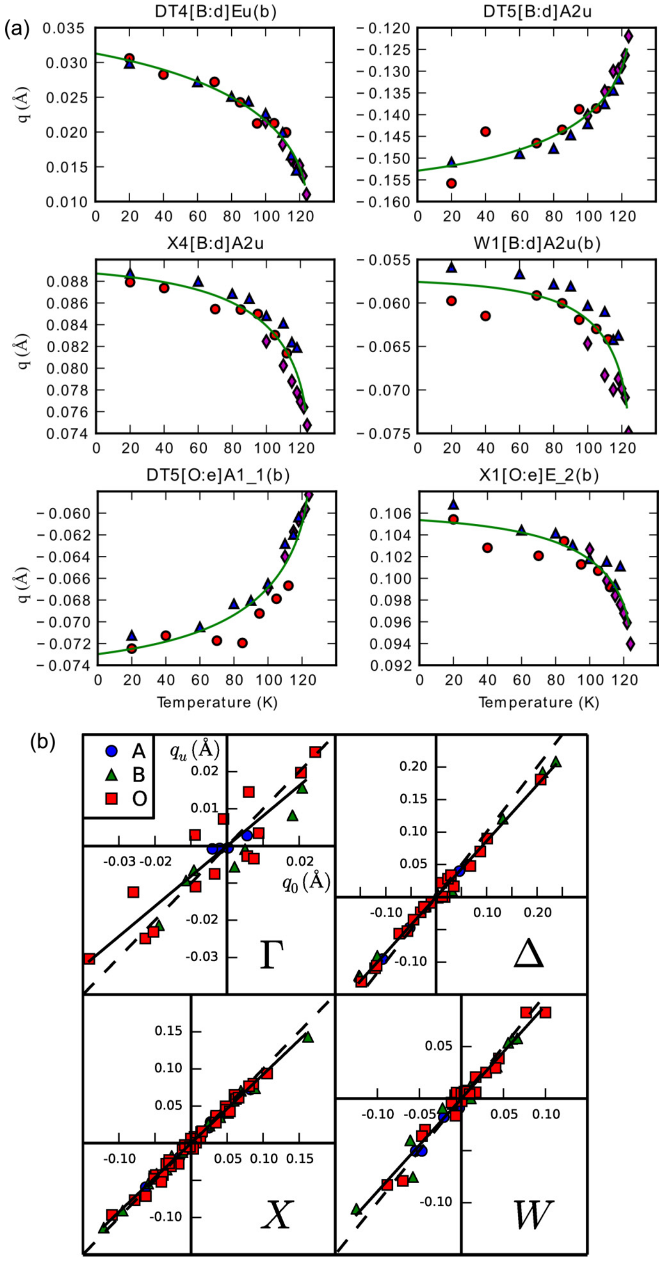

FIG. 4. (Color online) (a) Plots of representative frozen phonon mode amplitudes against temperature, showing fits of Eq. (3). Points shown as triangles/circles/diamonds are from refinements of Crystal 8/13/17 here and in Fig. 7(a). (b) Plot of $T = T_u$ against $T = 0$ values of the 168 frozen modes according to their symmetry class and the atom type (*A*- or *B*-site Fe, or O). The $q_u = q_0$ frozen limit (broken line) and the best-fit slope are shown on each plot.

D. Local modes: Charge and orbital order

Local distortion modes of the *B*-site FeO_6 octahedra are useful for exploring charge and orbital ordering as demonstrated previously [13]. The amplitude of the radial expansion or breathing mode Q_{Rad} (the change in octahedral average Fe-O bond distance compared to the structural average) with

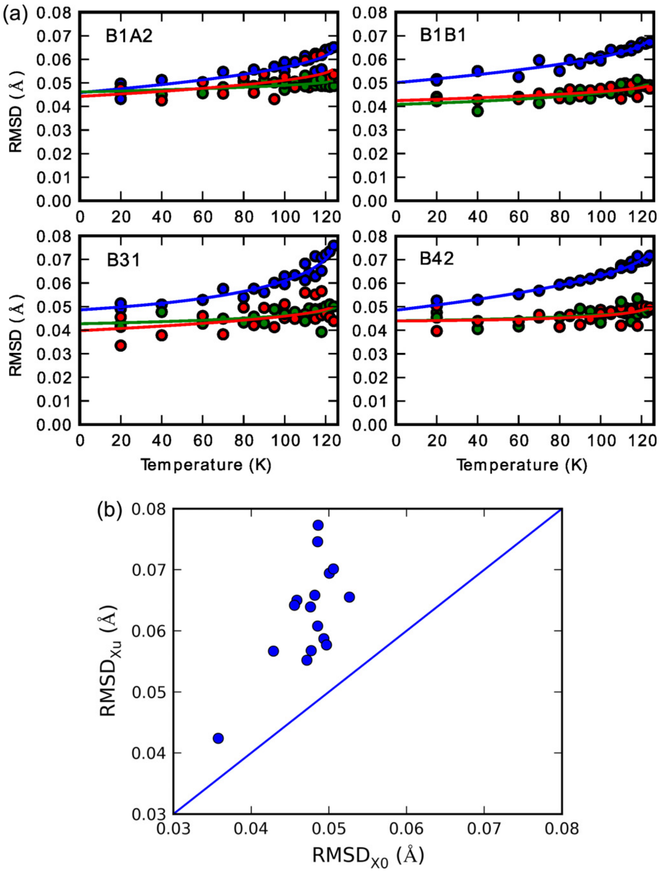

FIG. 5. (Color online) Root mean squared displacements (RMSDs) of B site Fe ions in the low-temperature magnetite structure. (a) Temperature variations of the three RMSDs for representative B sites as labeled, showing fits of Eq. (3). (b) Plot of $T = T_{\mathrm{u}}$ against $T = 0$ values of the largest RMSD for each of the 16 B sites. (B31 has the largest $T = T_{\mathrm{u}}$ value and B32 the smallest.) The $\mathrm{RMSD}_{\mathrm{u}} = \mathrm{RMSD}_0$ straight line shown corresponds to the frozen limit for the low-temperature structure.

A_{1g} symmetry is sensitive to charge order, as Fe^{2+} has a larger ionic radius than Fe^{3+}. The tetragonal E_g mode with amplitude Q_{JT} is found to describe the compressive Jahn-Teller distortion associated with orbital order of the degenerate high spin state of $3d^6$ Fe^{2+}, while the nondegenerate $3d^5$ configuration of Fe^{3+} is not Jahn-Teller active. The temperature variations of the Q_{Rad} and Q_{JT} local modes of the 16 B sites were fitted by Eq. (3) and the limiting values at $T = 0$ and T_{u} are shown on Fig. 6.

The $T = 0$ distribution of $(Q_{\mathrm{JT}}, Q_{\mathrm{Rad}})$ points is similar to that in the previous 90 K study and reveals the first-approximation charge ordering, as eight of the sites are Fe^{2+}-like with large Q_{Rad} and significantly negative Q_{JT} due to orbital ordering, while the eight Fe^{3+}-like sites have smaller Q_{Rad} and their Q_{JT} values are clustered around zero. However, Fig. 6 shows that the domains of the two charge states are much closer and almost overlap at T_{u}, demonstrating that a measurable segregation of charge occurs on cooling from T_{u} to zero temperature in the Verwey phase of magnetite. The $B1B2$ and $B31$ sites have almost identical $(Q_{\mathrm{JT}}, Q_{\mathrm{Rad}})$ values at T_{u}, but separate towards the Fe^{2+} and Fe^{3+} domains respectively on cooling. Evidence for an increase in charge order on cooling is that seven of the eight Fe^{3+} sites contract on cooling while six of the eight Fe^{2+} sites expand so that electron localization effects outweighs thermal contraction. The range of Q_{JT} values for Fe^{2+} sites does not change between T_{u} and zero temperature, but the Fe^{3+} range diminishes and six of the eight sites have a smaller magnitude of Q_{JT} at $T = 0$ than at T_{u}. This confirms that tetragonal E_g mode distortions for Fe^{2+}-like sites are intrinsic due to orbital order, whereas those for Fe^{3+} are imposed by the lattice distortion rather than a local electronic instability.

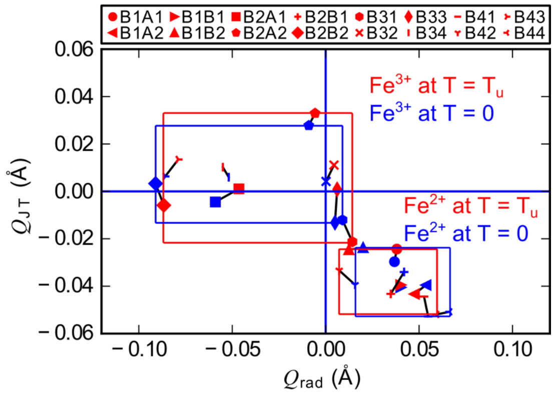

FIG. 6. (Color online) Plot of the local distortion mode amplitudes Q_{JT} against Q_{rad} showing the connected pair of extrapolated $T = 0$ and $T = T_{\mathrm{u}}$ points at for each of the 16 B sites in the Cc magnetite structure. Domains of the 8 Fe^{2+}-like and 8 Fe^{3+}-like sites at $T = 0$ and T_{u} are shown as rectangles.

E. *B*-*B* distances: Trimerons

The previous single-crystal study of magnetite at 90 K revealed structural distortions in addition to those from charge and orbital ordering, where distances from Fe^{2+} states to their two B-site neighbors in the local orbital ordering plane are anomalously shortened [13]. This demonstrates that the minority spin electrons are not fully localized as Fe^{2+} states but are instead spread over three sites within linear Fe-Fe-Fe units resulting in highly structured three-site polarons known as trimerons. Fourteen of the expected 16 trimeron contacts were found to be shorter than the average B-B distance.

The changes ΔD_{BB} of nearest-neighbor B-B distances relative to the value of 2.9677(1) Å in the cubic phase at 130 K are observed to increase in some cases but decrease for others on cooling in our refined structures, as shown in Fig. 7(a). The changes are parametrized through $T = 0$ and $T = T_{\mathrm{u}}$ values of ΔD_{BB}, obtained from fits of Eq. (3), and plotted in Fig. 7(b). This plot shows that the shortened B-B distances associated with the trimerons mostly contract further on cooling below T_{u} which is consistent with the increase in charge localization observed in Fig. 6. Longer B-B distances that are not involved in trimeron formation generally expand slightly on cooling. The largest expansion of 0.025 Å is for the nontrimeron $B2A1$-$B31$ contact, as a result of being at 180° to the trimeron $B31$-$B1B2$ distance, which shows the greatest contraction of 0.04 Å on cooling, as shown in Fig. 7(a). Fitted $\Delta D_{BB\mathrm{u}}/\Delta D_{BB0}$ slopes are 0.86 and 0.90 for trimeron and nontrimeron connections respectively, showing

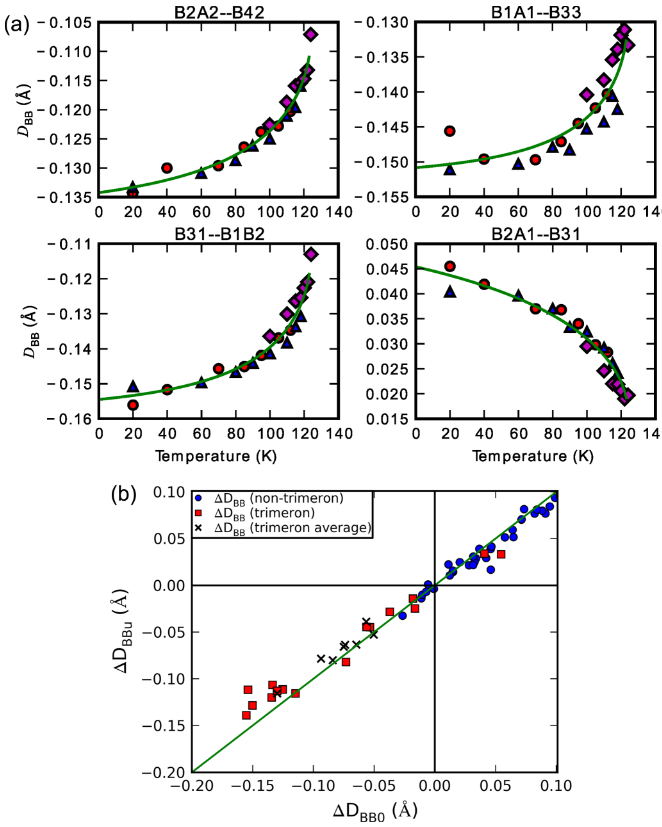

FIG. 7. (Color online) (a) Representative plots of changes in nearest-neighbor B-B distances ΔD_{BB} against temperature showing fits of Eq. (3). (b) Plot of $T = T_{\rm u}$ against $T = 0$ values of ΔD_{BB} with different symbols for trimeron and nontrimeron distances. Averages for the pair of B-B distances in each trimeron are also plotted. The $\Delta D_{BB{\rm u}} = \Delta D_{BB0}$ line shown corresponds to the frozen limit for the low-temperature structure.

that B-B distance changes below the Verwey transition are mainly driven by electron localization in trimerons. This is consistent with the changes in charge order in the Verwey phase noted in the previous section.

Most of the trimerons are distorted with unequal Fe-Fe distances within the linear Fe-Fe-Fe units due to the complex connectivity of trimerons. However, the mean values of $\Delta D_{BB{\rm u}}$ and ΔD_{BB0} for each trimeron lie in a relatively narrow range as shown on Fig. 7(b), confirming that the trimeron description of electron localization is consistent despite the dispersion in trimeron Fe-Fe distances.

IV. CONCLUSIONS

The spin, charge, orbital, and trimeron ordered ground state of magnetite represents perhaps the most complex electron ordering reported in transition-metal compounds, and has proved one of the most difficult to determine experimentally. This study demonstrates that the structural model reported from a previous microcrystal experiment at 90 K is accurate and reproducible, as 22 refinements from three further few-twin grains in the 10–40 μm size range give the same model between 20 K and $T_{\rm V}$ except for small differences due to thermal effects. The reproducibility of structural quantities such as those shown in Figs. 4 and 7(a) on a 10^{-3} Å scale is remarkable given the complexity of the structure and the twinning in all three microcrystals.

In keeping with previous studies of the Verwey transition, we find that the structural change is first order. The transition temperature for our highly stoichiometric magnetite sample is $T_{\rm c}(=T_{\rm V}) = 121.4$ K, and the upper limit observed for coexistence of the low- and high-temperature phases is $T_{\rm u} = 123.4$ K.

Determination of the critical exponent for variations in structural order parameters X with temperature approaching a first-order transition is difficult because the upper limiting value $X_{\rm u}$ is not known. We have found that the assumption of a mean-field-like $t_u^{1/2}$ variation works well here, and the function in Eq. (3) gives robust fitting over the entire temperature range below $T_{\rm u}$ with addition of only one fitting parameter W_X. The relations noted between W values for the cell parameter fits suggest that they carry some physical significance in allowing for the contribution of higher-order terms to the free-energy difference in Eq. (1). Comparison of X_0 and $X_{\rm u}$ order parameter values extrapolated to $T = 0$ and $T_{\rm u}$, respectively, is useful to discover how much thermal variation occurs within the low-temperature phase. For magnetite we find $X_{\rm u}/X_0 \approx 0.9$ so the low-temperature structural distortion is almost frozen below the Verwey transition. However, measurable thermal changes in some of the lattice and local mode amplitudes and B-B distances reveal an increase in electron localization on cooling. This is evidenced by increasing segregation of Fe^{2+}- and Fe^{3+}-type states according to their radial breathing and Jahn-Teller distortion modes, and further contraction of the B-B distances associated with trimeron bonding while other B-B distances tend to expand slightly on cooling. These changes emphasize that electron localization within trimerons is the driving force behind the Verwey transition, although their complex ordering pattern does not lead to simple relationships between the local trimeron distortions and the lattice distortions decomposed by symmetry modes. Electron localization within the Verwey phase is also revealed by anomalous decreases in the largest thermal displacement factors of the B-site cations, as electron-phonon decoupling occurs on cooling from $T_{\rm V}$ towards zero temperature.

ACKNOWLEDGMENTS

We thank Professor J. Honig for provision of the magnetite sample, EPSRC, ERC (European Research Council), and the Royal Commission for the Exhibition of 1851 for financial support, and STFC for provision of access to ESRF. We also thank Dr. A. Fitch and Dr. C. Drathen for assistance with powder data collection at beam line ID31.

---

[1] E. J. W. Verwey, Nature (London) **144**, 327 (1939).
[2] F. Walz, J. Phys. Condens. Matter **14**, R285 (2002).
[3] J. P. Attfield, J. Jpn. Soc. Powder Powder Metall. **61**, S43 (2014).
[4] M. Iizumi, T. F. Koetzle, G. Shirane, S. Chikazumi, M. Matsui, and S. Todo, Acta Crystallogr. Sect. B **38**, 2121 (1982).

[5] J. P. Wright, J. P. Attfield, and P. G. Radaelli, Phys. Rev. Lett. **87**, 266401 (2001).
[6] J. P. Wright, J. P. Attfield, and P. G. Radaelli, Phys. Rev. B **66**, 214422 (2002).
[7] J. Blasco, J. Garcia, and G. Subias, Phys. Rev. B **83**, 104105 (2011).
[8] R. J. Goff, J. P. Wright, J. P. Attfield, and P. G. Radaelli, J. Phys. Condens. Matter **17**, 7633 (2005).
[9] E. Nazarenko, J. E. Lorenzo, Y. Joly, J. L. Hodeau, D. Mannix, and C. Marin, Phys. Rev. Lett. **97**, 056403 (2006).
[10] Y. Joly, J. E. Lorenzo, E. Nazarenko, J. L. Hodeau, D. Mannix, and C. Marin, Phys. Rev. B **78**, 134110 (2008).
[11] S. R. Bland, B. Detlefs, S. B. Wilkins, T. A. Beale, C. Mazzoli, Y. Joly, P. D. Hatton, J. E. Lorenzo, and V. A. M. Brabers, J. Phys. Condens. Matter **21**, 485601 (2009).
[12] J. E. Lorenzo, C. Mazzoli, N. Jaouen, C. Detlefs, D. Mannix, S. Grenier, Y. Joly, and C. Marin, Phys. Rev. Lett. **101**, 226401 (2008).
[13] M. S. Senn, J. P. Wright, and J. P. Attfield, Nature (London) **481**, 173 (2012).
[14] J. P. Attfield, APL Mat. **3**, 041510 (2015).
[15] M. S. Senn, I. Loa, J. P. Wright, and J. P. Attfield, Phys. Rev. B **85**, 125119 (2012).
[16] M. S. Senn, J. P. Wright, and J. P. Attfield, J. Korean Phys. Soc. **62**, 1372 (2013).
[17] S. de Jong *et al.*, Nature Mater. **12**, 882 (2013).
[18] P. Novák, H. Štěpánková, J. Englich, J. Kohout, and V. A. M. Brabers, Phys. Rev. B **61**, 1256 (2000).
[19] A. C. Larson and R. B. Von Dreele, Los Alamos National Laboratory Report LAUR 86-748 (2000).
[20] B. H. Toby, J. Appl. Cryst. **34**, 210 (2001).
[21] Bruker, SMART and SAINT (Bruker AXS Inc., Madison, Wisconsin, USA, 1998).
[22] G. M. Sheldrick, Acta Crystallogr. A **64**, 112 (2008).
[23] See Supplemental Material at http://link.aps.org/supplemental/10.1103/PhysRevB.92.024104 for cif files from single-crystal structure refinements.
[24] E. K. H. Salje, *Phase Transitions in Ferroelastic and Co-elastic Crystals*, Cambridge topics in Mineral Physics and Chemistry No. 1 (Cambridge University Press, Cambridge, 1991).
[25] E. K. H. Salje, B. Wruck, and H. Thomas, H. Z. Phys. B **82**, 399 (1991).
[26] J. M. Honig, J. Alloys Compds. **229**, 24 (1995).
[27] R. S. Coe, R. Egli, S. A. Gilder, and J. P. Wright, Earth Planet. Sci. Lett. **319-320**, 207 (2012).
[28] J. P. Wright, A. M. T. Bell and J. P. Attfield, Solid State Sci. **2**, 747 (2000).
[29] We use here parametrization of the symmetry-adapted displacement as generated by pre-2011 versions of the ISODISTORT program (ISOTROPY Software Suite; iso.byu.edu; B. J. Campbell, H. T. Stokes, D. E. Tanner, and D. M. Hatch, J. Appl. Cryst. **39**, 607 (2006)) where mode amplitudes are given as the maximum displacements of an atom on the distortion mode generated according to irreducible representation tables (H. T. Stokes and D. M. Hatch, Isotropy Subgroups of the 230 Crystallographic Space Groups. (World Scientific, Singapore, 1988)) in which the basis vectors were nonorthogonal. We note that a more physical parametrization of the distortion modes in terms of the square root of the sum of the squares of the mode-induced changes in atomic displacement is implemented in more recent versions of ISODISTORT. This allows for a more direct comparison of the relative magnitudes of order parameters belonging to different irreducible representations. In this paper we have used the older parametrization for ease of comparison with our previously published work.
[30] G. Meissner and K. Binder, Phys. Rev. B **12**, 3948 (1975).